Biosensors and Bioelectronics 190 (2021) 113445

Contents lists available at ScienceDirect

Biosensors and Bioelectronics

journal homepage: www.elsevier.com/locate/bios

Photo-gated and self-powered three-dimensional DNA motors with boosted biostability for exceptionally precise and efficient tracing of intracellular *survivin* mRNA

Yu-Heng Liu [a,1], Jia-Ling Gao [a,1], Jun-Xian Liu [a], Da Liu [b], Wen-Kai Fang [b], Bei Zheng [c], Hong-Wu Tang [b,**], Cheng-Yu Li [a,*]

[a] Hubei Province Key Laboratory of Occupational Hazard Identification and Control, School of Public Health, Medical College, Wuhan University of Science and Technology, Wuhan, 430065, People's Republic of China
[b] College of Chemistry and Molecular Sciences, Wuhan University, Wuhan, 430072, People's Republic of China
[c] Westlake Institute for Advanced Study, School of Life Sciences, Westlake University, Hangzhou, 310024, People's Republic of China

ARTICLE INFO

Keywords:
DNA motor
Live cell
Photo-gated
Self-powered
Survivin mRNA

ABSTRACT

Benefiting from the outstanding signal amplification effect and the admirable construction flexibility, the currently proposed DNA motors (particularly DNA walkers) based biosensing concepts have provided a forceful fluorescence imaging tool for intracellular detection. Even so, this promising sensing means is not only subject to poor controllability and prone to produce false signals but also requires exogenous powering forces owing to the common employment of DNAzyme. In response to these challenges, we are herein motivated to present some meaningful solving strategies. For one thing, the surfaces of gold nanoparticles are conducted with a photo-gated walking behavior by introducing a photocleave mode, under which the light-switchable DNA walkers are capable of being selectively activated *via* an external ultraviolet source to faultlessly prevent the sensing frame from being pre-initiated during cellular uptake and intracellular delivery. For another, the intracellular biothiols are consumed by MnO_2 nanosheets to effectively avoid the competitions to Au–S bonds to eliminate potential false outputs and also self-supply sufficient cofactors (Mn^{2+}) to actualize a self-powered operation pattern as well as facilitate the endocytosis process. Following these breakthroughs, a favorable analysis performance towards a model tumor biomarker (*survivin* mRNA) is endowed with the newly raised biosensor, whose sensitivity is low to pM level with a sound specificity for identifying single base mismatching. Moreover, the significantly improved autonomous three-dimensional DNA walkers can be used to determine and dynamically trace the targets in live cancer cells with an exceptional precise and efficient manner, commendably impelling the sensing ability of DNA motors in biological specimens.

1. Introduction

DNA motors, due to their high sensitivity and good construction flexibility, have attracted a wide range of interests in biosensing field (Chang et al., 2019; Chen et al., 2020; Huang et al., 2019; Li et al. 2020a, 2020c; Liu et al., 2019; Lv et al., 2020; Peng et al. 2017, 2019; Qi et al., 2021; Skugor et al., 2019; Sun, 2017; Tang et al., 2020; Thubagere et al., 2017; Wang et al., 2017; Wen et al., 2019; Xu et al., 2016; Yang et al. 2016, 2019a, 2019b; Yin et al., 2020; Zhang et al., 2020a). As a rule, a conventional Watson-Crick base pairing principle is the most fundamental point for these DNA molecular systems and thus plentiful emerging concepts such as robots (Chang et al., 2019; Sun, 2017; Tang et al., 2020; Thubagere et al., 2017), tweezers (Li et al., 2020c; Yang et al., 2019b), wheels (Xu et al., 2016; Yang et al., 2019a), gears (Liu et al., 2019) and walkers (Chen et al., 2020; Huang et al., 2019; Peng et al. 2017, 2019; Qi et al., 2021; Skugor et al., 2019; Wang et al., 2017; Wen et al., 2019; Yang et al., 2016; Li et al., 2020a; Lv et al., 2020; Yin et al., 2020; Zhang et al., 2020a) have been designed. Among these sound choices, DNA walkers possess a more convenient signal amplification effect by means of a step-wise mechanical movement along a

* Corresponding author.
** Corresponding author.
E-mail addresses: hwtang@whu.edu.cn (H.-W. Tang), li-chengyu@wust.edu.cn (C.-Y. Li).
[1] Yu-Heng Liu and Jia-Ling Gao contributed equally to this work.

https://doi.org/10.1016/j.bios.2021.113445
Received 11 May 2021; Received in revised form 3 June 2021; Accepted 12 June 2021
Available online 16 June 2021

pre-programmed track. To further promote the surface loading and simultaneously enhance the mobile efficiency, the focus is gradually shifted from the early developed low-dimensional walkers to the present three-dimensional (3D) walking behavior, and this extended sensing means has exhibited a favorable application potential in a variety of live specimens (*e.g.* cells) after employing it as a fluorescence imaging tool (Chen et al., 2020; Lv et al., 2020; Peng et al., 2017; Wang et al., 2017; Wen et al., 2019; Zhang et al., 2020a). Although much efforts have been made to realize the analysis of intracellular metal ions (Wang et al., 2017), nucleic acids (Lv et al., 2020; Peng et al., 2017; Wen et al., 2019; Zhang et al., 2020a) and proteins (Chen et al., 2020), such attractive strategy still suffers from the following challenges.

On one hand, owing to the reason that a majority of sensing targets are widely distributed within cellular media, some necessary processes such as endocytosis and intracellular delivery will inevitably pre-initiate the programmed walking process in an uncontrollable way (Lubbe et al., 2017). Affected by this inherent defect, the captured fluorescence signals are unable to truly reflect the actual target abundance corresponding to the spatial location where the biosensors finally arrive at. Therefore, the existing fluorescent DNA walkers are almost entirely lack of satisfying assay accuracy and seeking an effective pathway to break through this bottleneck is of great urgency. Encouragingly, an innovative light activation triggered photo-gated manner which is capable of significantly enhancing the precision of target recognition (Chu et al., 2019; Li et al., 2020b; Yang et al., 2018; Zhao et al. 2018, 2019) can fulfill this goal. Normally, this light-switching phenomenon is induced by integrating a *O*-nitrobenzyl (or its derivatives) composed photocleavage linker (PC-linker) into the sensing frame (Yang et al., 2018; Zhao et al., 2019). Based on this handling, the improved biosensors can be selectively activated to respond the targets only in the irradiation of an external simple ultraviolet (UV) light. Following this, not only a perfectly controlled walking behavior is rendered but also the imaging resolution in space and time is dramatically strengthened (Chu et al., 2019; Zhao et al., 2018). Very Recently, Zhang et al. (2020a) incorporated such photo-gated concept into DNA walkers by combining with an upconversion luminescence based fluorescence ratio method for intracellular imaging. However, the complicated synthesis process of nanocarriers and the use of multiple light sources are not an ideal option.

On the other hand, in view of the common usage of metal ions dependent DNAzymes to touch off the walking behavior, whether the powering forces (that are cofactors) are adequate is a precedent concerning. To ensure this, the shortage of endogenous cofactors is usually compensated by supplying with extra metal ions (Peng et al., 2017; Lv et al., 2020). But unfortunately, this uncertain supplement not only leads to a more complex sensing operation but also potentially cause adverse influence to the physiological activities of live cells (Mathad et al., 2006). In addition, considering most of the proposed walking routes are often anchored onto the surfaces of gold nanoparticles (AuNPs) *via* Au–S bonds, the conjugated DNA strands are very likely to undergo forceful competitions between various intracellular biothiols (especially high concentration GSH) and such ligand exchange reaction will probably break the biological conjugation to produce false signals and finally reduce the sensing reliability. Although few advanced studies demonstrated that Au–Se bonds are an available selection (Gao et al., 2018; Hu et al., 2018), the selenol modified nucleic acids are difficult to obtain and this drawback is not conductive to design DNA based sensing frame. Thus, establishing a self-powered notion and concurrently overcoming background outputs are quite vital.

Inspiringly, thanks to the enormous progress of nanoscience, a kind of currently discovered two-dimensional nanomaterial which is MnO_2 nanosheets is promising to resolve these obstacles (Fan et al., 2015; Ou et al., 2017; Sha et al., 2019; Wang et al., 2019a). Profiting from the outstanding oxidation ability, MnO_2 nanosheets can be dissociated by many reducing substances to yield large amounts of Mn^{2+}. Moreover, some researches (Ou et al., 2017; Wang et al. 2019a, 2019b) also exhibit that the large specific surface area and the strong physical adsorption capacity towards DNA nucleobases can make MnO_2 nanosheets act as a commendable nanocarrier to facilitate the efficiency of cellular uptake and such merit will endow a better intracellular imaging ability. However, the unique property of Mn^{2+} release and the excellent resistance to consume intracellular biothiols are not utilized in these reports. Upon further integrating these additional features into DNA walkers, not only the walking behavior can be provided with self-supplied powering forces but also allowing the sensing frame own superior biostability.

Motivated by the hints above, we present here a photo-gated and self-powered autonomous 3D DNA walker with boosted biostability. For this brand-new fluorescent biosensor, a UV light is employed to activate the walking behavior and MnO_2 nanosheets are exploited to offer intrinsic powering forces as well as improve working adaptability in biological media. As a proof-of-investigation, the intact DNA walkers supported biosensor is served as an effective imaging tracer for precisely and sensitively determining intracellular *survivin* mRNA, a type of short messenger RNA (24 nt) which has been confirmed to be highly associated with various malignant tumors (Ratajczak et al., 2018; Stobiecka et al., 2019). The specific construction steps and the intracellular operation principle is displayed in Scheme 1 (detailed nucleic sequences are shown in Table S1), in which a long walking strand (73 nt) embedded with a Mn^{2+}-dependent DNAzyme is first locked by a PC-linker modified locking strand, and then the locked walking strand and FAM labelled substrate strands (33 nt) are jointly conjugated onto the surface of a AuNP to fabricate a photo-gated DNA walker (termed as PGW). As such, a noteworthy fluorescence resonance energy transfer (FRET) mechanism will happen to the ideally paired energy bodies to quench the FAM emissions. After assembling the PGWs onto a MnO_2 nanosheet (termed as PGWs/M), the nanocomposite is availably endocytosis by a lysosome and escape to enter into the cytoplasm. At this time, the MnO_2 nanosheet will be dissociated by a redox reaction with intracellular GSH (whereby the GSH is transformed into GSSG) to generate sufficient Mn^{2+} and also discharge the PGWs. Once applying a moderate 365 nm UV light to irradiate the cell, the "c + b" part of locking strand is released from the hybridization structure and the detection targets will induce a toehold strand displacement effect towards the remaining double chain. By making use of the exposed walking strand to conduct the RNA cleavage of DNAzyme under the self-supplied cofactors, the initiated walking behavior will eventually restore the as-quenched fluorescence signals. In order to fully explore the capability to monitor the variations of intracellular targets, this highly integrated biosensor is also used to analyze biochemical agents regulated live cancer cells. On the whole, our efforts can offer a meaningful sensing concept for propelling the application of DNA motors in bioimaging.

2. Experimental section

2.1. Synthesis of AuNPs

Before this experiment, all glassware should be soaked in freshly-prepared aqua regia (V_{HCl}/V_{HNO3} = 3:1) overnight and washed fully with deionized water. First, 2.06 mL of 1% $HAuCl_4$ was added into a 100 mL round-bottom flask containing 47.94 mL of deionized water and the mixture was kept vigorous stirring for 5 min. Then, the yellowish solution was heated to 120 °C in an oil bath and 5 mL of 38.8 mM freshly-prepared sodium citrate dihydrate was poured into the flask at once. After maintaining the warm for about 1 min, it can be clearly seen that the solution color was turned into dark red. Upon heating for another 10 min, the flask was allowed to cool to room temperature, followed by purifying the final solution with a 220 nm Millipore membrane filter for twice. For long-term preservation, the as-obtained AuNPs with wine red were stored at 4 °C in a dark environment and the actual concentration was calculated to be approximately 4 nM by using an ultraviolet–visible (UV–Vis) spectrometric approach, wherein the extinction coefficient of 13 nm AuNPs is $2.7 \times 10^8\ M^{-1}cm^{-1}$ (Liu et al., 2011).

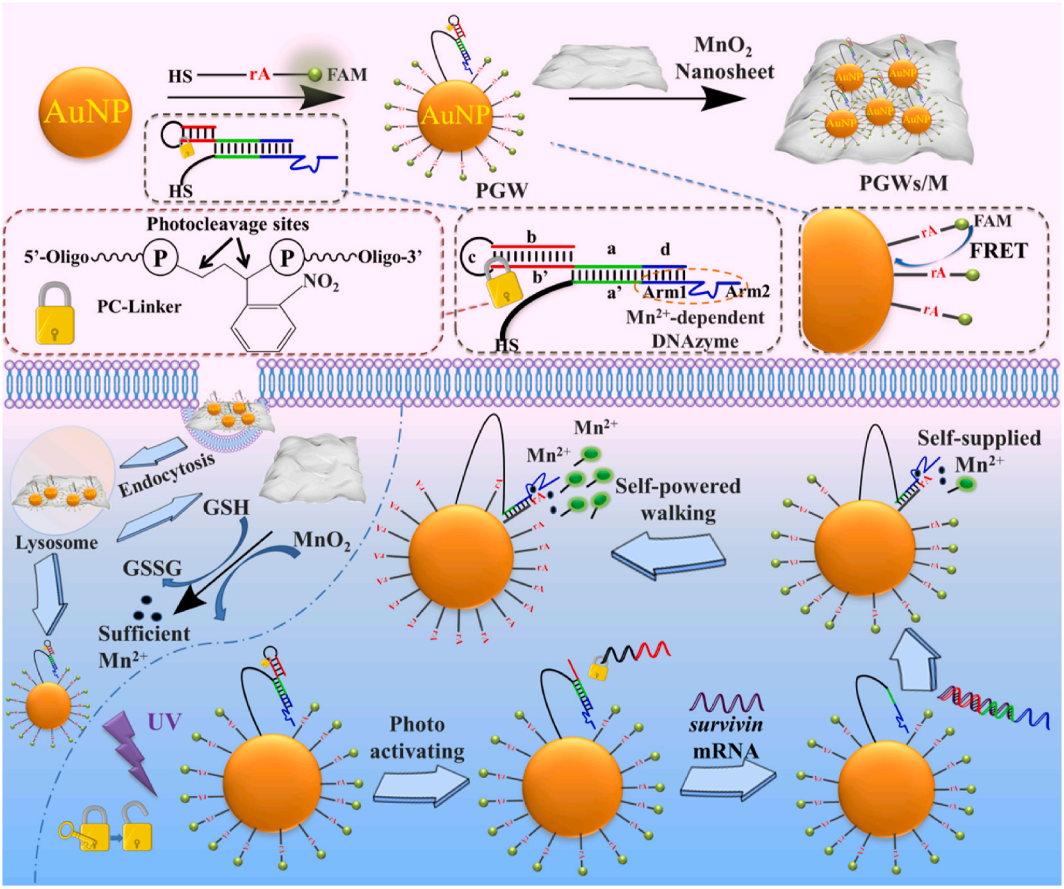

Scheme 1. Specific construction steps and the intracellular operation principle (not in a real scale) of photo-gated, self-powered and biostability boosted autonomous 3D DNA walkers.

2.2. Preparation of PGWs

20 μL of PBS solution (10 mM, pH 7.4, 200 mM NaCl) containing a specific molar ratio of walking/locking strands (1:3, which can realize a perfect locking effect to perform the photo-gated manner) was first heated to 95 °C for 5 min and then quickly transferred to a −20 °C refrigerator to cool for at least 5 min. Next, 0.05 nmol of the as-locked walking strand and 0.75 nmol of substrate strand were treated with 5 mM tris(2-carboxyethyl)phosphine overnight, respectively, followed by stirring gently with 4 nM AuNPs in a thermostatic shaker at 37 °C, during which a certain amount of 0.5% Tween-20 and 0.7 M NaCl were added separately. The former was able to prevent the aggregation of AuNPs and the latter was used to increase the loading efficiency of DNA strands. Once maintaining the moderate incubation for another 24 h, centrifugal treatment (16000 g for 20 min) was performed to remove the unconjugated strands and the obtained PGWs was washed several times with deionized water. To regulate an approximate working concentration for subsequent experiment, the final PGWs were resuspended into 300 μL of Tris-HCl buffer solution (25 mM, pH 7.4) *via* ultrasonic processing (concentration ~ 2 nM) and stored at 4 °C.

2.3. Synthesis of MnO_2 nanosheets

At first, 3% H_2O_2 and 0.6 M tetramethylammonium hydroxide were fully mixed together in a 50 mL round-bottom flask at room temperature. After providing with certain amounts of deionized water to maintain the total volume at 20 mL, the mixture was added with 10 mL of 0.3 M $MnCl_2{\cdot}4H_2O$. In a very short time, the original clear solution would become dark brown due to the oxidization of Mn^{2+}. Once maintaining the vigorous stirring in an open air for another 14 h, the black cloudy solution was centrifuged at 2000 g for 10 min and the resulting bulks were washed in sequence with deionized water and ethanol, followed by drying thoroughly in a 60 °C oven. To prepare MnO_2 nanosheets solution, 10 mg of the obtained black bulks were dispersed into 20 mL of deionized water and further processed with ultrasound for at least 10 h. Finally, centrifugal treatment (2000 g for 10 min) was performed to remove large size particles and the collected supernatant was kept at 4 °C for long-term preservation.

2.4. Preparation of PGWs/M

3.6 μL of 500 μg/mL MnO_2 nanosheets, 30 μL of 2 nM PGWs and 26.4 μL of Tris-HCl buffer solution (40 mM, pH 7.4) were mixed together *via* vortex in a 1.5 mL tube at room temperature for 60 min, followed by progressively introducing 200 mM NaCl for three times to reinforce the physical absorption between PGWs and MnO_2 nanosheets. After incubating gently for another 2 h, the resulting PGWs/M were washed three times with deionized water and the final concentration was defined at 1 nM according to the addition of AuNPs.

3. Results and discussion

3.1. Preparation route and gradual characterization of PGWs/M

According to our fabrication procedures (Fig. 1A), a AuNP is first synthesized by employing a classical citrate reduction method (Saha et al., 2012) and then a PGW is prepared by collectively conjugating substrate strands and a locked walking strand onto the surface of AuNP through forceful Au–S bindings. After that, a MnO_2 nanosheet created by the chemical oxidation of Mn^{2+} using tetramethylammonium cations

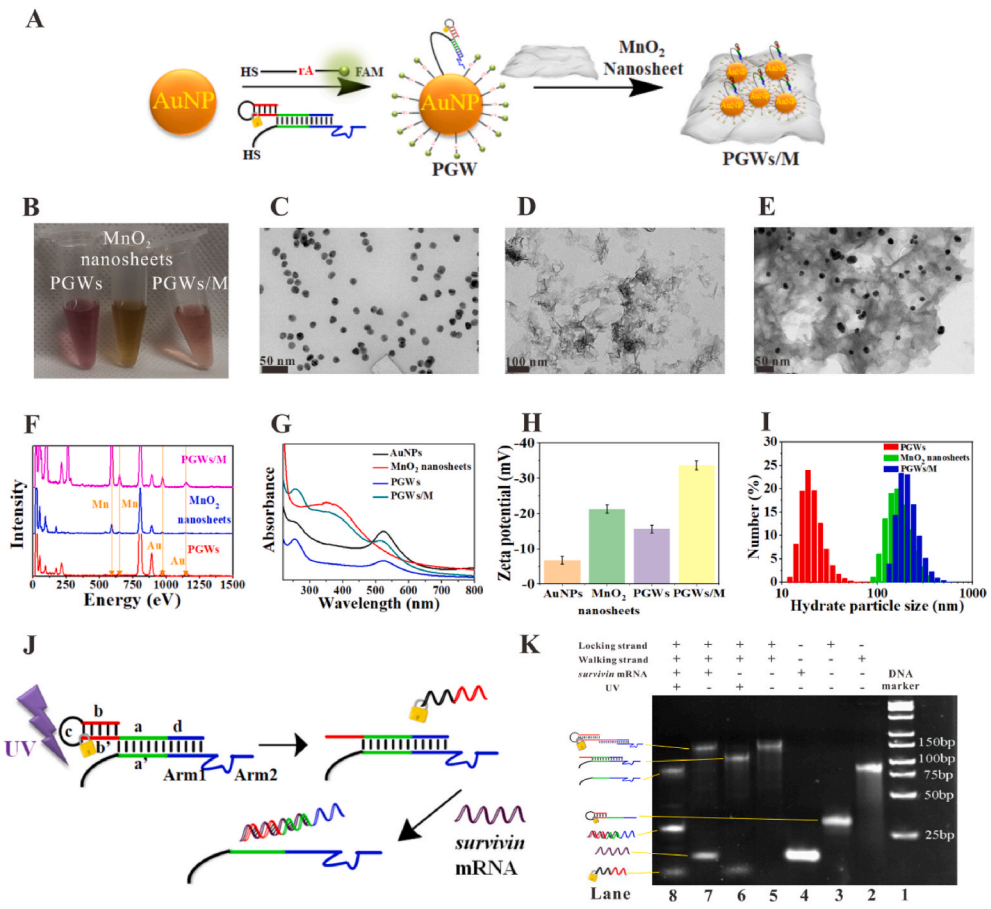

Fig. 1. (A) Fabrication procedures (not in a real scale) of PGWs/M. (B) Digital images of PGWs (2 nM), MnO_2 nanosheets (30 μg/mL) and PGWs/M (1 nM) dispersed in deionized water. (C)–(E) TEM images of PGWs (scale bar is 50 nm), MnO_2 nanosheets (scale bar is 100 nm) and PGWs/M (scale bar is 50 nm). (F) EDS lines of PGWs, MnO_2 nanosheets and PGWs/M. (G) UV–Vis adsorption spectra of AuNPs, MnO_2 nanosheets, PGWs and PGWs/M. (H) Zeta potentials of AuNPs, MnO_2 nanosheets, PGWs and PGWs/M. (I) Hydrate particle sizes of PGWs, MnO_2 nanosheets and PGWs/M. (J) Schematic illustration of photo-gated manner induced toehold strand displacement effect in the co-existence of UV light and *survivin* mRNA. (K) 10% PAGE demonstration of photo-gated manner. Lanes 1–8: 25–500 bp marker, walking strand, locking strand, *survivin* mRNA, walking strand + locking strand, walking strand + locking strand + UV, walking strand + locking strand + *survivin* mRNA, walking strand + locking strand + *survivin* mRNA + UV, respectively.

(Zhao et al., 2013) is exploited to physically adsorb the internal single stranded DNAs of PGWs to form the final nanocomposite (PGWs/M).

Such preparation route can be clearly demonstrated by the naked eye *via* the changes of solution colors (Fig. 1B), among which a mixed color assigned to the wine red of PGWs and the brown of MnO_2 nanosheets is exhibited to PGWs/M. The corresponding morphologies are uncovered by a battery of transmission electron microscopy (TEM) images, from which spherical-like shapes with excellent dispersibilities are vested in AuNPs (Fig. S1) and PGWs (Fig. 1C), along with slice layers are presented to MnO_2 nanosheets (Fig. 1D). Of note, a number of PGWs will be visibly attached onto the basal planes of MnO_2 nanosheets upon realizing the assembly process (Fig. 1E), suggesting the successful formation of nanocomposites. The average sizes of these nanostructures are also revealed by sequential size statistical histograms (n = 250), for which no significant variations come to the combination of DNA strands (13.65 nm and 13.79 nm for AuNPs and PGWs, respectively, Figs. S2A and S2B) and the physical absorption case (152.18 nm and 154.36 nm for MnO_2 nanosheets and PGWs/M, respectively, Figs. S2C and S2D). The definite distributions of metal elements for the as-adopted synthetic pathway are substantiated by energy-dispersive X-ray spectroscopy (EDS) records (Fig. 1F), in which the featured energy lines of Au and Mn appear concurrently in the nanocomposites. UV–Vis adsorption spectra (Fig. 1G) primely confirms a highly efficient bioconjugation event and an evident assembly result. For the former, other than the common peak position (~520 nm) of 13 nm AuNPs (Saha et al., 2012), a new characteristic absorption centered at 260 nm belonging to nucleic acid molecules (Li et al., 2019) occurs in PGWs. For the latter, PGWs/M gives an additional appearance of a wide peak at around 340 nm, a typical optical property for MnO_2 based nanomaterials (Fan et al., 2015; Zhao et al., 2013). These inferences are able to be further attested by dynamic light scattering data, wherein the bimolecular loading and the physical assembly phenomenon are not only endowed with a distinct decline trend to the Zeta potentials (Fig. 1H) but also show a slight broadening to the hydrate particle sizes (Fig. 1I).

3.2. Feasibility of photo-gated manner and Mn^{2+}-dependent RNA cleavage

In principle, we need to pay close attention to the following concerns before establishing the desired DNA walkers. For one thing, whether the UV light induced toehold strand displacement effect (Fig. 1J) can be actualized is a prerequisite. For this purpose, polyacrylamide gel electrophoresis (PAGE) investigation is then conducted. As displayed in Fig. 1K, owing to the fact that the connection between the ends of PC-linker and the adjacent bases are completely cut off, the hairpin chain ("c + b" part) of locking strand is efficiently released from the hybridization structure and a slightly longer migration distance will be emerged after illuminating the locked walking strand with a 365 nm UV lamp (lane 6). Because the unreleased chain ("b'+a+d" part) which partially complementary to the Mn^{2+}-dependent DNAzyme has a stronger affinity towards *survivin* mRNA, the remaining locking strand will preferentially bind to the target (lane 8), whereas no double stranded band is produced without the treatment of this activation light (lane 7). Hence, the as-proposed photo-gated manner can be fully guaranteed under the irradiation of a UV light.

For another, since Mn^{2+} should be served as the cofactor to trigger the RNA cleavage of DNAzyme and finally initiate the walking behavior, the expectant cleavage mechanism is also inspected roundly. In the presence of Mn^{2+}, it is observed from the PAGE analysis (Fig. S3) that the substrate strand is finely degraded, indicating that Mn^{2+} is capable of inserting into the loop structure (between arm 1 and arm 2 in Fig. 1J) of DNAzyme to perform the enzymatic catalysis at the rA position of

substrate strand. To certify the influence of Mn^{2+} concentration in more detail, a Mn^{2+}-dependent DNAzyme and a double modified (FAM and BHQ-1) substrate strand are annealed to construct an elaborate FRET system (Fig. S4A) and fluorescent study is next executed. In Fig. S4B, an obvious Mn^{2+} reliant sign is rendered and the recovered FAM emissions will reach a balance point when the treated [Mn^{2+}] is at 500 μM.

3.3. Assessing the most efficient walking behavior

By virtue of these precedent verifications, we began to assess the most efficient walking behavior by making use of exogenous powering forces assisted photo-gated DNA walkers (Fig. 2A) under the optimized reaction conditions (*e.g.* pH: 7.4, temperature: 37 °C and ion strength: 200 mM NaCl, Fig. S5). First, the concentration ratio between substrate strand and locked walking strand is an important factor for this walking process. For this reason, various ratios (5:1 to 30:1) are introduced into the sensing frame and it can be found that the quenching efficiencies (as high as 88%) are almost equal for all cases (Fig. S6A). However, owing to the steric hindrance for the coupled DNA strands (Zhang et al. 2020a, 2020b), the signal recovery abilities are optimal when the ratio is selected at 15:1 (Fig. S6B).

Second, considering the demand of enough unlocked walking strands to ensure an effective walking behavior on AuNPs, the potential correlation with the UV light is testified. As anticipated, such progressive walking pattern is entirely in a silence state without the activation of this gated light while a pronounced fluorescence recovery event arises to the co-existence of target (Fig. S7). Beyond that, it is seen from Fig. 2B that the longer irradiation time (power density ~ 2.5 W/cm^2) is greatly beneficial to the signal recovery capacity, for which 10 min of processing time will lead to the most conspicuous intensity, implying that a maximum of substrate strands is degraded in this case.

Third, on account of the truth that the powering forces are supplied by Mn^{2+}, the Mn^{2+} concentration is crucial to the working performance of this extrinsic powered biosensor. Such conjecture is commendably proved by the results of fluorescence kinetic validation (Fig. 2C), from which the increasing presence of Mn^{2+} can in favor of a more remarkable walking behavior and this tendency will also attain to a plateau by treating with 500 μM cofactor. Besides, a relatively rapid response is assigned to such photo-gated DNA walkers and the real-time fluorescence intensities will reach saturation in 30 min for all testing groups. Aside from these findings, profiting from the exclusive binding interaction of DNAzyme (Hwang et al., 2019), the biosensor owns an outstanding ion selectivity towards other nonspecific metallic (*e.g.* Zn^{2+}, Mg^{2+}, Ca^{2+}, K^+, Na^+, Fe^{2+}, Fe^{3+} and Al^{3+}) and nonmetallic (*e.g.* NH_4^+) cations (Fig. S8).

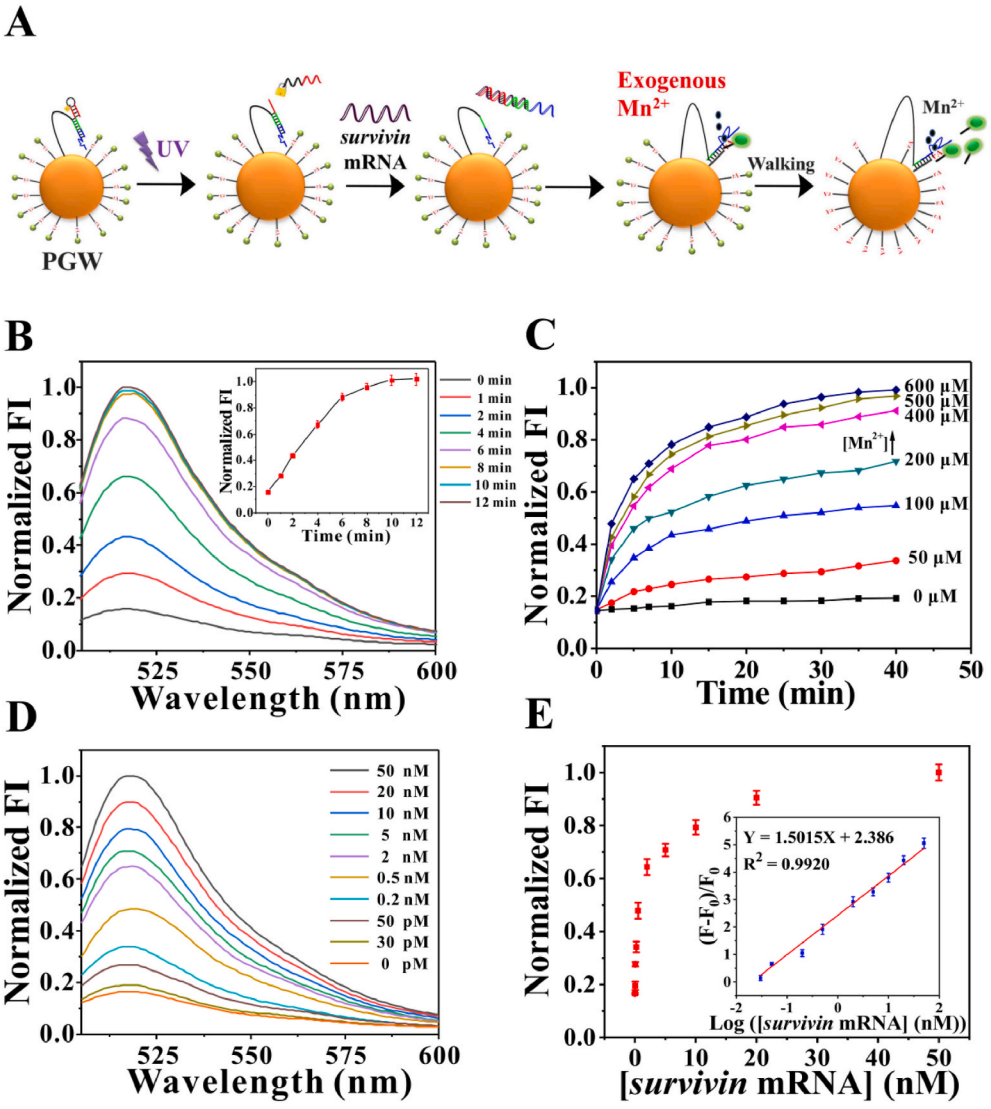

Fig. 2. (A) Extracellular sensing principle (not in a real scale) of PGWs supported biosensor under the supplement of sufficient exogenous Mn^{2+}. (B) Fluorescence recovery of the biosensor under different irradiation time of 365 nm UV light (0 min–12 min, power density ~ 2.5 W/cm^2, 500 μM Mn^{2+}, 50 nM *survivin* mRNA). Inset: correlation between normalized fluorescence intensity (selecting 12 min UV light irradiation time as the highest signal point) and irradiation time. (C) Fluorescence kinetic validation (0 min–40 min) of the biosensor by treating with different amounts of Mn^{2+} (0 μM–600 μM). Normalized FI: selecting [Mn^{2+}] and treating time are severally 600 μM and 40 min as the highest signal point. (D) Normalized fluorescence spectra (selecting 50 nM target concentration as the highest signal point) of the biosensor in response to different concentrations of *survivin* mRNA (0 pM–50 nM). (E) Scatter plot of normalized FI versus target concentration. Inset: working curve ranging from 30 pM to 50 nM between relative fluorescence intensity ($(F–F_0)/F_0$, which means recovery ratio to blank signal) and logarithm of [*survivin* mRNA]. All error bars represent standard deviations of three independent experiments.

3.4. Evaluating extracellular sensing ability of PGWs supported biosensor

Under the above optimized walking conditions, we then carefully evaluate the extracellular sensing ability by utilizing the PGWs supported biosensor towards standard *survivin* mRNA. Fig. 2D illustrates that the incremental addition of targets ranging from 30 pM to 50 nM will bring about a more noteworthy fluorescence recovery phenomenon to the as-quenched FAM signals. By further exploring the underlying working curve between the relative fluorescence intensity ($(F–F_0)/F_0$, where F and F_0 severally represent the fluorescence intensity in the presence and absence of *survivin* mRNA) and the logarithm of [*survivin* mRNA], it comes to a follow that the former (that is the recovery ratio to blank signal) shows a strict linear relationship spanning three orders of magnitude with the latter (R^2: 0.9920, Fig. 2E). In accordance with the routine 3σ/k (where σ and k separately indicate the standard deviation of blank sample determined from eleven parallel tests and the slope of linearity curve) based calculation criterion, a limit of detection (LOD) as low as 25.6 pM is estimated to this sensing approach. Such favorable sensitivity resulting from the DNA walkers assured signal amplification not only holds forceful competitiveness to other reported fluorescent intracellular RNA biosensors (Table S2) but also is afford to face with the detection of intracellular *survivin* mRNA (Ratajczak et al., 2018).

Except for the exploration of sensitivity, specificity is another pivotal issue due to the fact that plentiful homologues exist in the family of messenger RNA. To this end, the PGWs supported biosensor is utilized in response to single-to-three base mismatching cases (referred as M1, M2 and M3) and other nonspecific substances including a random RNA (referred as R), four proteins (alpha fetal protein (AFP), carcinoembryonic antigen (CEA), bovine serum albumin (BSA) and prostate-specific antigen (PSA)) and a representative small molecule (adenosine 5′-triphosphate (ATP)). The examination results are displayed in Fig. S9, from which the introduction of targets can give rise to the most prominent fluorescence recovery manner ($P < 0.001$). Ascribing to the reason that the crescent mismatched bases will gradually reduce the efficiency of strand displacement (Simmel et al., 2019), the detectable signals for M1, M2 and M3 are markedly decreased to occupy 52% ($P < 0.001$), 21% ($P < 0.001$) and 12% ($P < 0.001$) of the target group, respectively. More than that, in light of the impossible identification events, the rest of examined biomolecules can hardly make contributions to restore the quenched fluorescence and their relative intensities display no significant difference ($P > 0.05$) to the blank signal. Overall, the newly developed biosensor possesses vitally satisfactory specificity which even enable to differentiate the variation of single base, laying a good foundation for the latter intracellular sensing.

3.5. Evaluating extracellular sensing ability of PGWs/M supported biosensor

Following the favorable sensing ability by manually providing sufficient Mn^{2+}, the self-powered walking behavior using PGWs/M is next demonstrated under the reducibility of GSH (Fig. 3A). In consideration of the concentration range of intracellular GSH (normally 1–10 mM) (Fan et al., 2015; Duthie et al., 1988), a focus arises to whether the abundance of such internal biothiols can effectively dissociate the MnO_2 nanosheets to discharge the PGWs. Fortunately, the complete disappearance of MnO_2 absorption spectra (Fig. 3B) indicates that only a very small amount of MnO_2 nanosheets (30 μg/mL) is qualified for consuming 1 mM GSH and this redox reaction will bring about a

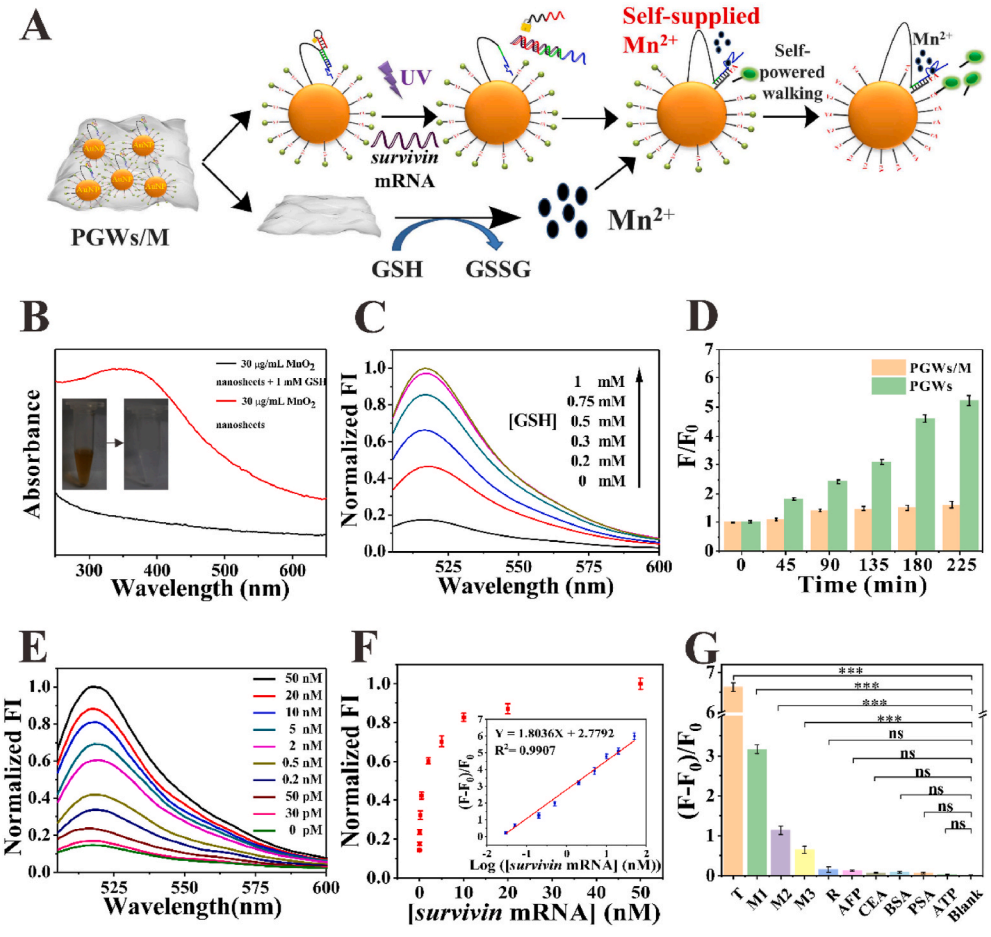

Fig. 3. (A) Extracellular sensing principle (not in a real scale) of PGWs/M supported biosensor by introducing MnO_2 nanosheets to self-supply Mn^{2+}. (B) UV–Vis adsorption spectra of 30 μg/mL MnO_2 nanosheets in the presence and absence of 1 mM GSH. Inset: digital images of solution color change (left: MnO_2 nanosheets, right: MnO_2 nanosheets + GSH). (C) Fluorescence recovery of the biosensor under different concentrations of GSH (0 mM–1 mM). Normalized FI: selecting 1 mM GSH as the highest signal point. (D) Investigation of background outputs for PGWs and PGWs/W supported biosensors (in the absence of *survivin* mRNA) by introducing with 10 mM GSH. F_0 indicates initial fluorescence intensity (0 min) of corresponding biosensor. F indicates fluorescence intensity of corresponding biosensor with time evolution (0 min–225 min). (E) Normalized fluorescence spectra (selecting 50 nM target concentration as the highest signal point) of the biosensor in response to different concentrations of *survivin* mRNA (0 pM–50 nM). (F) Scatter plot of normalized FI versus target concentration. Inset: working curve ranging from 30 pM to 50 nM between relative fluorescence intensity ($(F–F_0)/F_0$, which means recovery ratio to blank signal) and logarithm of [*survivin* mRNA]. (G) Specificity examination determined by $(F–F_0)/F_0$ towards M1, M2, M3, R, AFP, CEA, BSA, PSA and ATP. All error bars represent standard deviations of three independent experiments. $^{***}P < 0.001$, ns: no significant difference ($P > 0.05$). (For interpretation of the references to color in this figure legend, the reader is referred to the Web version of this article.)

transparent solution within 1 min (Fig. 3B, inset). After incubating the PGWs/M supported biosensor with different amounts of GSH (0 mM–1 mM), it can be acquired a saturated fluorescence signal when the incubated [GSH] is set at 0.75 mM (Fig. 3C), primely suggesting that the GSH in cells is enough to produce plenty of Mn^{2+} to accomplish the self-supplied walking operation. Apart from this, because of the disturbing competitive reactions between various biothiols and Au–S bonds in biological media, the resistance of PGWs and PGWs/M toward high concentration GSH (10 mM) are also compared in the absence of targets. Thanks to the resultful consumption of MnO_2 nanosheets to GSH, the PGWs/M system appears only weak background outputs even treated for as long as 225 min while a progressive fluorescence ascent comes to the PGWs system after 45 min (Fig. 3D).

Having confirmed the feasibility of introducing MnO_2 nanosheets, the sensing ability of PGWs/M supported biosensor is investigated as well in the photo-gated manner. Benefiting from the sufficient powering forces stemmed from the dissociation of MnO_2 nanosheets, the fluorescence recovery trend ranging from 30 pM to 50 nM (Fig. 3E), the linear relation curve (R^2: 0.9907, Fig. 3F, LOD ~19.6 pM) as well as the specificity (Fig. 3G) show negligible fluctuations to that of the pure PGWs case, revealing that the self-powered DNA walkers not only integrally maintain the original detection performance but also in possession of a simpler automated operation mode.

3.6. Sensing survivin mRNA in live cancer cells

Prior to achieving this goal, the possible toxicities of UV light source and nanocomposites toward cell viabilities need to be taken into account thoroughly. On the strength of methyl thiazolyl tetrazolium based determinations, it is found that the quite moderate light power density has no apparent adverse impact on the growth states of two model cancer cell lines (HeLa and MCF-7) under the optimal irradiation time (Fig. S10). In addition to the above, by reason of the intrinsic hypotoxicity of MnO_2 matrices and AuNPs, the viabilities of these cells are kept as high as 87% even though the PGWs/M concentration is up to 2 nM (Fig. S11). Moreover, the cellular uptake of PGWs/M is expressly evidenced by lysosome tracking experiment (Fig. S12), in which the faultless colocalization to the FAM signals manifests that the biosensor is ultimately delivered to the cytoplasm.

As expected, very effective photo-gated results in live cancer cells are endowed with our sensing strategy, by which the two types of cell lines incubated with 1 nM PGWs/M for 4 h are hard to capture distinct fluorescence signals without the employments of UV lights to activate the biosensor (Fig. 4A and B, **top images**). In stark to this unactivated

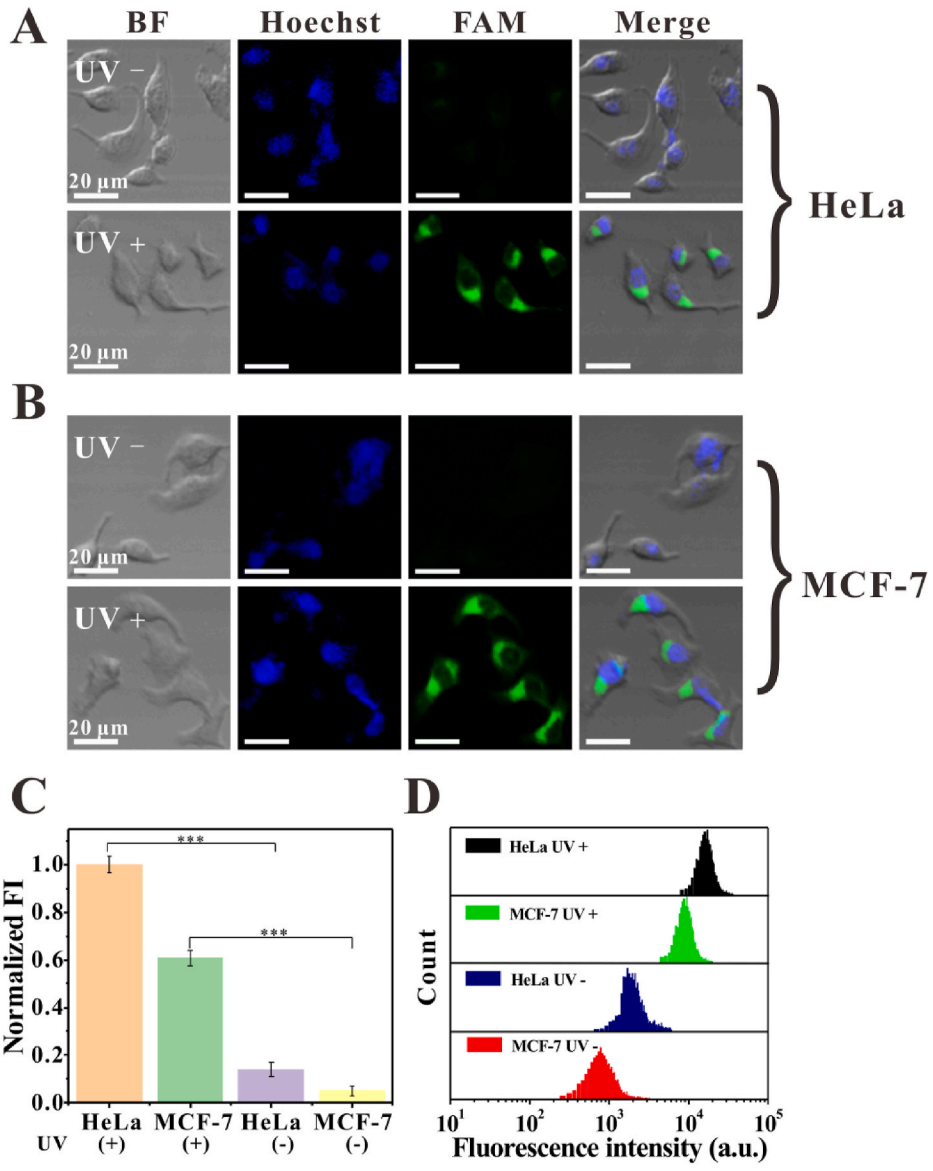

Fig. 4. (A)–(B) Top: confocal fluorescence images (scale bars are 20 μm) of live HeLa cells by incubating with PGWs/M (1 nM) in PBS solution (25 mM, pH 7.4, 200 mM NaCl) for 4 h (in the absence of UV light irradiation). Bottom: confocal fluorescence images (scale bars are 20 μm) of live MCF-7 cells by incubating with PGWs/M (1 nM) in PBS solution (25 mM, pH 7.4, 200 mM NaCl) for 4 h and treating with UV light irradiation (power density ~ 2.5 W/cm^2). Signal acquisition channels and exposure time are 520 ± 30 nm and 200 ms, respectively. (C) Quantified normalized fluorescence intensities (selecting UV light treated HeLa cells as the highest signal point) from these confocal images through an Image-J software. Error bars represent standard deviations of three independent experiments. ***$P < 0.001$. (D) Fluorescence intensity distributions determined by flow cytometry measurements, wherein 10^4 digested cells are counted in each case.

phenomenon, arresting FAM signals caused by the walking behavior triggered fluorescence recovery are given rise to the treatment of UV irradiation at the same exposure time (Fig. 4A and B, **bottom images**). Upon applying an Image-J software to analyze these confocal images (Fig. 4C), it is obtained that the quantified intensities for these activation cases are 6.1-fold (HeLa cells, $P < 0.001$) and 10.2-fold (MCF-7 cells, $P < 0.001$) higher than the corresponding untreated groups, respectively, together with a finding that the mean FAM signals of HeLa cells are approximately 1.67 times to the MCF-7 cells. Additionally, it is worth pointing out that the consumption of biothiols *via* MnO_2 nanosheets does prevent the biosensor from generating false signals in this live biological sample whether there is UV activation (Fig. S13) or not (Fig. S14). Meanwhile, flow cytometry measurements are carried out to inspect the data accuracy, wherein a perfectly consistent relationship is exhibited (Fig. 4D). Furthermore, the distinguishable *survivin* mRNA levels are finely in keeping with the relative quantification data obtained from reverse transcription polymerase chain reaction (RT-PCR) assay (Fig. S15) and it is very likely put down to the heavily expressed nature of this template RNA in cervical tumors (Temme et al., 2007).

3.7. Dynamic tracing intracellular survivin mRNA

With a view to this next-generation cancer biomarker, developing a reliable and precise intracellular sensing means for actualizing dynamic trace can offer useful information about tumorigenesis and progression for clinical diagnosis (Ratajczak et al., 2018; Stobiecka et al., 2019). To accomplish to this task, the photo-gated and self-powered DNA walkers supported biosensor is finally acted as an imaging tracer for detecting *survivin* mRNA in live HeLa cells with different physiological states. Regarding to this application, the intracellular targets are down-regulated with certain amounts of sepantronium bromide (denoted as YM155, a class of *survivin* inhibitor) (Chandrasekaran et al., 2020). Compared with the control cells (untreated case, Fig. 5A, **top image**), the increasing introduction of YM155 will lead to much weaker FAM signals (Fig. 5A, **middle and bottom images**), implying that the downgrade targets are not conductive to the walking efficiency. Furthermore, the brightness of these confocal images is reduced by 32% ($P < 0.001$) and 50% ($P < 0.001$) for 1.5 nM and 3 nM reagents mediated cases (Fig. 5B), respectively. Likewise, such fluorescence decline sign is explained well by flow cytometry data (Fig. 5C) and the variations of intracellular *survivin* mRNA are also proved by RT-PCR analysis (Fig. S16). Therefore, this highly integrated fluorescent biosensor has outstanding tracing adaptability in live specimens.

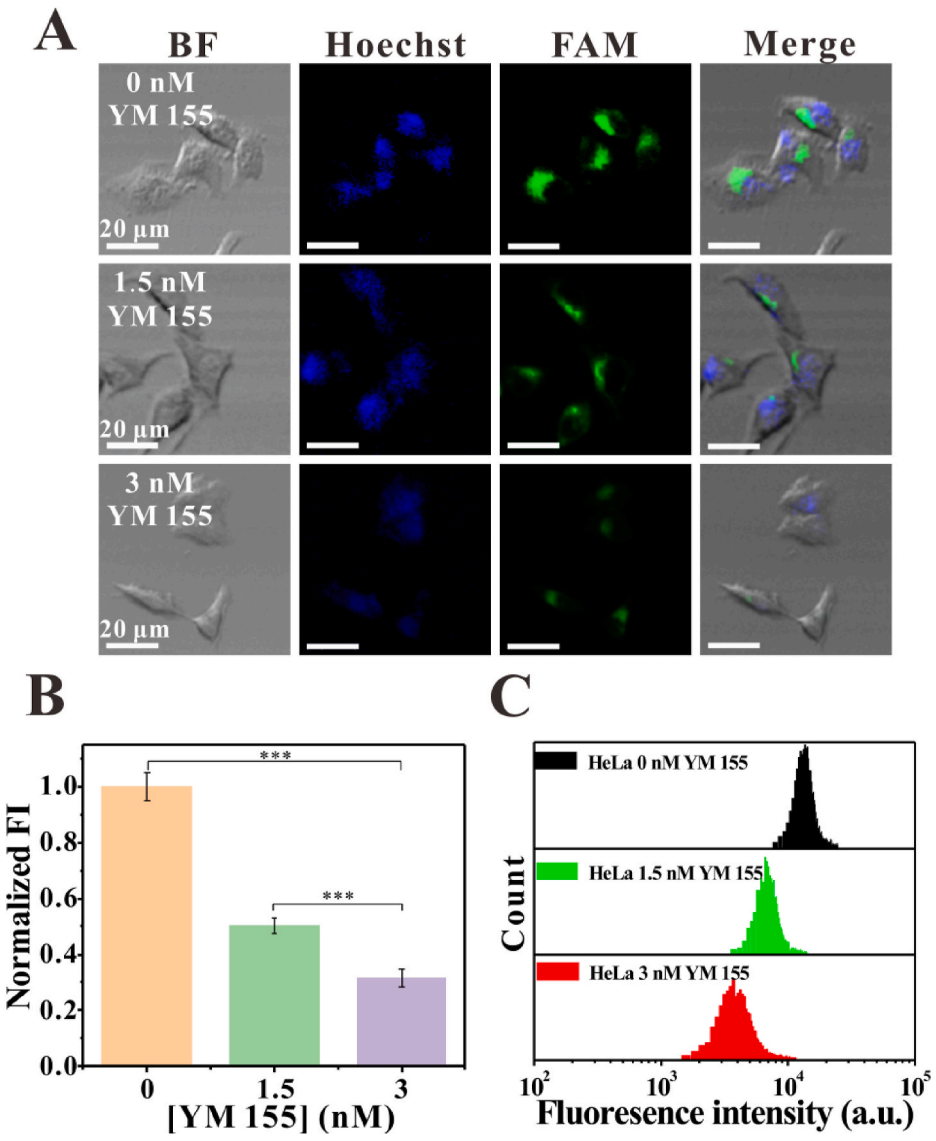

Fig. 5. (A) Confocal fluorescence images (scale bars are 20 μm) of YM 155 (0 nM, 1.5 nM and 3 nM) treated live HeLa cells by incubating with PGWs/M (1 nM) in PBS solution (25 mM, pH 7.4, 200 mM NaCl) for 4 h and treating with UV light irradiation (power density ~ 2.5 W/cm^2). Signal acquisition channels and exposure time are 520 ± 30 nm and 200 ms, respectively. (B) Quantified normalized fluorescence intensities (selecting untreated HeLa cells as the highest signal point) from these confocal images through an Image-J software. Error bars represent standard deviations of three independent experiments. ***$P < 0.001$. (C) Fluorescence intensity distributions determined by flow cytometry measurements, wherein 10^4 digested cells are counted in each case.

4. Conclusions

Unlike the present reported 3D DNA walkers, an exceptional photogated and self-powered autonomous operation pattern is proposed in this work. With the assistance of the light-switching mode, our walking behavior is able to be initiated to recognize the targets in a fully controllable manner through the irradiation of a simple 365 nm UV light source (power density is as low as 2.5 W/cm^2). After utilizing MnO_2 nanosheets to carry the newly constructed DNA walkers and consume the intracellular biothiols (*e.g.* GSH), the fluorescent biosensor not only possesses a better endocytosis and a potent biostability but also can self-supply sufficient Mn^{2+} to ensure adequate self-powered forces. By further designing a traditional FRET based "off-to-on" signal readout, this novel detection strategy shows a satisfactory analysis performance towards *survivin* mRNA, for which no obvious fluctuations in sensitivity (LODs are at around ~ 20 pM) and specificity (enabling identify single-base mismatching) are found to the presence and absence of the self-supplied cofactors. Taking advantage of these useful improvements, we can precisely and efficiently execute imaging and monitoring assays in live cancer cells (*e.g.* HeLa and MCF-7) and the determined target levels are well documented by other gold-standard methods such as flow cytometry and RT-PCR, opening up an attractive venue for DNA motors in biosensing field.

CRediT authorship contribution statement

Yu-Heng Liu: Methodology, Validation, Investigation, Writing – original draft. **Jia-Ling Gao:** Methodology, Validation, Investigation. **Jun-Xian Liu:** Validation, Investigation. **Da Liu:** Validation, Investigation. **Wen-Kai Fang:** Validation, Investigation. **Bei Zheng:** Validation, Investigation. **Hong-Wu Tang:** Project administration, Funding acquisition. **Cheng-Yu Li:** Conceptualization, Methodology, Writing – original draft, Writing – review & editing, Visualization, Supervision, Project administration, Funding acquisition.

Declaration of competing interest

The authors declare that they have no known competing financial interests or personal relationships that could have appeared to influence the work reported in this paper.

Acknowledgments

This work was supported by the National Natural Science Foundation of China (21904102, 81772256 and 21827808).

Appendix A. Supplementary data

Supplementary data to this article can be found online at https://doi.org/10.1016/j.bios.2021.113445.

References

Chandrasekaran, A.P., Poondla, N., Ko, N.R., Oh, S.J., Ramakrishna, S., 2020. YM155 sensitizes HeLa cells to TRAIL-mediated apoptosis via cFLIP and survivin downregulation. Oncol. Lett. 20 (4), 72.

Chang, Y.Y., Wu, Z.Y., Sun, Q.X., Zhuo, Y., Chai, Y.Q., Yuan, R., 2019. Simply constructed and highly efficient classified cargo-discharge DNA robot: a DNA walking nanomachine platform for ultrasensitive multiplexed sensing. Anal. Chem. 91 (13), 8123–8128.

Chen, K., Huang, Q., Fu, T., Ke, G.L., Zhao, Z.B., Zhang, X.B., Tan, W.H., 2020. MicroRNA-initiated and intracellular Na^+-Fueled DNAzyme motor for differentiating molecular subtypes of nonsmall cell lung cancer. Anal. Chem. 92 (11), 7404–7408.

Chu, H.Q., Zhao, J., Mi, Y.S., Zhao, Y.L., Li, L.L., 2019. Near-infrared light-initiated hybridization chain reaction for spatially and temporally resolved signal amplification. Angew. Chem. Int. Ed. 58 (42), 14877–14881.

Duthie, S.J., Coleman, C.S., Grant, M.H., 1988. Status of reduced glutathione in the human hepatoma-cell line, hep-G2. Biochem. Pharmacol. 37 (17), 3365–3368.

Fan, H.H., Zhao, Z.L., Yan, G.B., Zhang, X.B., Yang, C., Meng, H.M., Chen, Z., Liu, H., Tan, W.H., 2015. A smart DNAzyme-MnO_2 nanosystem for efficient gene silencing. Angew. Chem. Int. Ed. 54 (16), 4801–4805.

Gao, X.N., Jiang, L.L., Hu, B., Kong, F.P., Liu, X.J., Xu, K.H., Tang, B., 2018. Au-Se-Bond-Based nanoprobe for imaging MMP-2 in tumor cells under a high-thiol environment. Anal. Chem. 90 (7), 4719–4724.

Hu, B., Kong, F.P., Gao, X.N., Jiang, L.L., Li, X.F., Gao, W., Xu, K.H., Tang, B., 2018. Avoiding thiol compound interference: a nanoplatform based on high-fidelity Au-Se bonds for biological applications. Angew. Chem. Int. Ed. 57 (19), 5306–5309.

Huang, J., Zhu, L.Y., Ju, H.X., Lei, J.P., 2019. Telomerase triggered DNA walker with a superhairpin structure for human telomerase activity sensing. Anal. Chem. 91 (11), 6981–6985.

Hwang, K., Mou, Q.B., Lake, R.J., Xiong, M.Y., Holland, B., Lu, Y., 2019. Metal-dependent DNAzymes for the quantitative detection of metal ions in living cells: recent progress, current challenges, and latest results on FRET ratiometric sensors. Inorg. Chem. 58 (20), 13696–13708.

Li, C.Y., Kang, Y.F., Qi, C.B., Zheng, B., Zheng, M.Q., Song, C.Y., Guo, Z.Z., Lin, Y., Pang, D.W., Tang, H.W., 2019. Breaking through bead-supported assay: integration of optical tweezers assisted fluorescence imaging and luminescence confined upconversion nanoparticles triggered luminescent resonance energy transfer (LRET). Anal. Chem. 91 (12), 7950–7957.

Li, C.Y., Zhang, T., Kang, Y.F., Qi, C.B., Zheng, B., Xu, C.M., Lin, Y., Pang, D.W., Tang, H. W., 2020a. Incorporating luminescence-concentrating upconversion nanoparticles and DNA walkers into optical tweezers assisted imaging: a highly stable and ultrasensitive bead supported assay. Chem. Commun. 56 (51), 6997–7000.

Li, C.Y., Zheng, B., Kang, Y.F., Tang, H.W., Pang, D.W., 2020b. Integrating 808 nm light-excited upconversion luminescence powering with DNA tetrahedron protection: an exceptionally precise and stable nanomachine for intracelluar MicroRNA tracing. ACS Sens. 5 (1), 199–207.

Li, J.J., Wang, W.J., Zhang, H., Lu, Z.C., Wu, W.X., Shu, M.B., Han, H.Y., 2020c. Programmable DNA tweezer-actuated SERS probe for the sensitive detection of AFB (1). Anal. Chem. 92 (7), 4900–4907.

Liu, D.B., Wang, Z., Jiang, X.Y., 2011. Gold nanoparticles for the colorimetric and fluorescent detection of ions and small organic molecules. Nanoscale 3 (4), 1421–1433.

Liu, X., Zhang, J.J., Fadeev, M., Li, Z.Y., Wulf, V., Tian, H., Willner, I., 2019. Chemical and photochemical DNA "gears" reversibly control stiffness, shape-memory, self-healing and controlled release properties of polyacrylamide hydrogels. Chem. Sci. 10 (4), 1008–1016.

Lubbe, A.S., Szymanski, W., Feringa, B.L., 2017. Recent developments in reversible photoregulation of oligonucleotide structure and function. Chem. Soc. Rev. 46 (4), 1052–1079.

Lv, S.Z., Zhang, K.Y., Zhu, L., Tang, D.P., 2020. ZIF-8-Assisted NaYF4:Yb,Tm@ZnO converter with exonuclease III-powered DNA walker for near-infrared light responsive biosensor. Anal. Chem. 92 (1), 1470–1476.

Mathad, P., Uttam, V.G., Mathad, R.D., 2006. Interactive effect of metal ions over exponential growth period of microalgal cells. J. Environ. Biol. 27 (2), 413–417.

Ou, M., Huang, J., Yang, X.H., Quan, K., Yang, Y.J., Xie, N.L., Wang, K.M., 2017. MnO2 nanosheet mediated "DD-A" FRET binary probes for sensitive detection of intracellular mRNA. Chem. Sci. 8 (1), 668–673.

Peng, H.Y., Li, X.F., Zhang, H.Q., Le, X.C., 2017. A microRNA-initiated DNAzyme motor operating in living cells. Nat. Commun. 8, 14378.

Peng, X., Wen, Z.B., Yang, P., Chai, Y.Q., Liang, W.B., Yuan, R., 2019. Biomimetic 3D DNA nanomachine via free DNA walker movement on lipid bilayers supported by hard SiO_2@CdTe nanoparticles for ultrasensitive MicroRNA detection. Anal. Chem. 91 (23), 14920–14926.

Qi, Y., Zhai, Y.Q., Fan, W.J., Ren, W., Li, Z.P., Liu, C.H., 2021. Click chemistry-actuated digital DNA walker confined on a single particle toward absolute MicroRNA quantification. Anal. Chem. 93 (3), 1620–1626.

Ratajczak, K., Krazinski, B.E., Kowalczyk, A.E., Dworakowska, B., Jakiela, S., Stobiecka, M., 2018. Hairpin-hairpin molecular beacon interactions for detection of survivin mRNA in malignant SW480 cells. ACS Appl. Mater. Interfaces 10 (20), 17028–17039.

Saha, K., Agasti, S.S., Kim, C., Li, X.N., Rotello, V.M., 2012. Gold nanoparticles in chemical and biological sensing. Chem. Rev. 112 (5), 2739–2779.

Sha, H.F., Zhang, Y., Wang, Y.F., Ke, H., Xiong, X., Jia, N.Q., 2019. Electrochemiluminescence resonance energy transfer biosensor between the glucose functionalized MnO_2 and g-C_3N_4 nanocomposites for ultrasensitive detection of concanavalin A. Biosens. Bioelectron. 124, 59–65.

Simmel, F.C., Yurke, B., Singh, H.R., 2019. Principles and applications of nucleic acid strand displacement reactions. Chem. Rev. 119 (10), 6326–6369.

Skugor, M., Valero, J., Murayama, K., Centola, M., Asanuma, H., Famulok, M., 2019. Orthogonally photocontrolled non-autonomous DNA walker. Angew. Chem. Int. Ed. 58 (21), 6948–6951.

Stobiecka, M., Ratajczak, K., Jakiela, S., 2019. Toward early cancer detection: focus on biosensing systems and biosensors for an anti-apoptotic protein survivin and survivin mRNA. Biosens. Bioelectron. 137, 58–71.

Sun, W.J., 2017. DNA robots that sort cargoes DNA. Nat. Nanotechnol. 12 (12), 1120-1120.

Tang, J.P., Yao, C., Gu, Z., Jung, S.W., Luo, D., Yang, D.Y., 2020. Super-soft and super-elastic DNA robot with magnetically driven navigational locomotion for cell delivery in confined space. Angew. Chem. Int. Ed. 59 (6), 2490–2495.

Temme, A., Rodriguez, J.A., Hendruschk, S., Gunes, S., Weigle, B., Schakel, K., Schmitz, M., Bachmann, M., Schackert, G., Rieber, E.P., 2007. Nuclear localization of Survivin renders HeLa tumor cells more sensitive to apoptosis by induction of p53 and Bax. Canc. Lett. 250 (2), 177–193.

Thubagere, A.J., Li, W., Johnson, R.F., Chen, Z.B., Doroudi, S., Lee, Y.L., Izatt, G., Wittman, S., Srinivas, N., Woods, D., Winfree, E., Qian, L.L., 2017. A cargo-sorting DNA robot. Science 357 (6356). No. eaan6558.

Wang, W.J., Satyavolu, N.S.R., Wu, Z.K., Zhang, J.R., Zhu, J.J., Lu, Y., 2017. Near-infrared photothermally activated DNAzyme-gold nanoshells for imaging metal ions in living cells. Angew. Chem. Int. Ed. 56 (24), 6798–6802.

Wang, J., Wang, D.X., Tang, A.N., Kong, D.M., 2019a. Highly integrated, biostable, and self-powered DNA motor enabling autonomous operation in living bodies. Anal. Chem. 91 (8), 5244–5251.

Wang, S., Wang, L., Xu, X.W., Li, X., Jiang, W., 2019b. MnO2 nanosheet-mediated ratiometric fluorescence biosensor for MicroRNA detection and imaging in living cells. Anal. Chim. Acta 1063, 152–158.

Wen, Z.B., Peng, X., Yang, Z.Z., Zhuo, Y., Chai, Y.Q., Liang, W.B., Yuan, R., 2019. A dynamic 3D DNA nanostructure based on silicon-supported lipid bilayers: a highly efficient DNA nanomachine for rapid and sensitive sensing. Chem. Commun. 55 (89), 13414–13417.

Xu, J.G., Wu, Z.S., Wang, Z.M., Li, H.L., Le, J.Q., Jia, L., 2016. Two-wheel drive-based DNA nanomachine and its sensing potential for highly sensitive analysis of cancer-related gene. Biomaterials 100, 110–117.

Yang, X.L., Tang, Y.A., Mason, S.D., Chen, J.B., Li, F., 2016. Enzyme-powered three-dimensional DNA nanomachine for DNA walking, payload release, and biosensing. ACS Nano 10 (2), 2324–2330.

Yang, Z.L., Loh, K.Y., Chu, Y.T., Feng, R.P., Satyavolu, N.S.R., Xiong, M.Y., Huynh, S.M. N., Hwang, K., Li, L.L., Xing, H., Zhang, X.B., Chelma, Y.R., Gruebele, M., Lu, Y., 2018. Optical control of metal ion probes in cells and zebrafish using highly selective DNAzymes conjugated to upconversion nanoparticles. J. Am. Chem. Soc. 140 (50), 17656–17665.

Yang, F., Cheng, Y.R., Cao, Y., Zhang, Y.Y., Dong, H.F., Lu, H.T., Zhang, X.J., 2019a. MicroRNA triggered DNA "nano wheel" for visualizing intracellular microRNA via localized DNA cascade reaction. Anal. Chem. 91 (15), 9828–9835.

Yang, W.T., Shen, Y., Zhang, D.Y., Li, C., Yuan, R., Xu, W.J., 2019b. Programmed dual-functional DNA tweezer for simultaneous and recognizable fluorescence detection of microRNA and protein. Anal. Chem. 91 (12), 7782–7789.

Yin, Y.M., Chen, G.F., Gong, L., Ge, K.Z., Pan, W.Z., Li, N., Machuki, J.O., Yu, Y.Y., Geng, D.Q., Dong, H.F., Gao, F.L., 2020. DNAzyme-powered three-dimensional DNA walker nanoprobe for detection amyloid beta-peptide oligomer in living cells and in vivo. Anal. Chem. 92 (13), 9247–9256.

Zhang, E., Zhang, Y., Zhang, X.B., Li, Y.Y., He, Y.L., Liu, Y., Ju, H.X., 2020a. A photo zipper locked DNA nanomachine with an internal standard for precise miRNA imaging in living cells. Chem. Sci. 11 (24), 6289–6296.

Zhang, H., Xu, X.W., Jiang, W., 2020b. An interparticle relatively motional DNA walker and its sensing application. Chem. Sci. 11 (28), 7415–7423.

Zhao, G.X., Li, J.X., Ren, X.M., Hu, J., Hu, W.P., Wang, X.K., 2013. Highly active MnO2 nanosheet synthesis from graphene oxide templates and their application in efficient oxidative degradation of methylene blue. RSC Adv. 3 (31), 12909–12914.

Zhao, J., Gao, J.H., Xue, W.T., Di, Z.H., Xing, H., Lu, Y., Li, L.L., 2018. Upconversion luminescence-activated DNA nanodevice for ATP sensing in living cells. J. Am. Chem. Soc. 140 (2), 578–581.

Zhao, J., Chu, H.Q., Zhao, Y., Lu, Y., Li, L.L., 2019. A NIR light gated DNA nanodevice for spatiotemporally controlled imaging of MicroRNA in cells and animals. J. Am. Chem. Soc. 141 (17), 7056–7062.